
BORN-SERIES-INSPIRED RESIDUAL METRIC FOR LEARNING-BASED PRECONDITIONERS

A PREPRINT

Juntao Wang^{a,c}, Xinliang Liu^b, Jiwei Jia^{a,c*}

^a School of Mathematics, Jilin University, Changchun 130012, China

^b Ocean University of China, Qingdao 266100, China

^c Shenzhen Loop Area Institute, Shenzhen 518038, China

jiajiwei@jlu.edu.cn

ABSTRACT

Loss functions for learning-based PDE preconditioners implicitly choose a *metric* in which residuals are matched, yet most approaches still optimize an unpreconditioned Euclidean residual norm. For indefinite operators such as the high-frequency Helmholtz equation, this default metric can make both learning and iterative correction overly sensitive to near-resonant spectral components, while classical preconditioning succeeds precisely by reshaping the residual geometry. We show that the Born Series and shifted-Laplacian left preconditioning are linked by the identity $I - G_\eta V_\eta = G_\eta A = L_\eta^{-1} A$, which turns the reference Green operator G_η into a natural Riesz-map residual metric $R_\eta = G_\eta^* G_\eta$ and suggests measuring the physical residual via $\|r\|_{R_\eta} = \|G_\eta r\|_2$. Building on this viewpoint, we propose a *Neural Preconditioned Born Series* (NPBS) iteration that replaces the scalar CBS relaxation with a residual-driven neural operator, together with a metric-matched Born-series-inspired loss $\mathcal{L}_{\text{bs}}^{R_\eta}$. The framework is architecture-agnostic and supports fast $\mathcal{O}(N \log N)$ evaluation via FFT/DST/DCT. Numerical experiments on heterogeneous Helmholtz problems demonstrate the effectiveness of our method, and its advantage becomes more pronounced as the systems grow more ill-conditioned; we then extend the framework to other PDE classes, including convection–diffusion–reaction equations and linearized Newton systems for nonlinear PDEs, where it also yields substantial iteration reductions.

Keywords Born Series · Neural preconditioner · Residual metric

1 Introduction

The heterogeneous Helmholtz equation remains challenging for both classical and learning-based solvers in high-wavenumber and high-contrast regimes. Standard discretizations suffer from pollution errors Babuška and Sauter [1997]; multilevel methods face coarse-grid dispersion mismatch Stolk [2016]; and indefiniteness degrades relaxation and coarse correction Ernst and Gander [2011]. A variety of classical remedies: shifted-Laplacian preconditioning Erlangga et al. [2004], wave-ray multigrid Brandt and Livshits [1997], Livshits and Brandt [2006], convergent Born series (CBS) Osnabrugge et al. [2016], and domain decomposition Chen and Xiang [2013], Leng and Ju [2022]—have improved robustness, yet efficiency in strongly heterogeneous media is still not fully resolved. Learning-based PDE solvers have progressed from PINNs Raissi et al. [2019] to neural operators Azzadenesheli et al. [2024], Lu et al. [2021], Li et al. [2020, 2022], Rahman et al. [2022], He et al. [2024], Cao [2021], He et al. [2025], Cao et al. [2025]. For Helmholtz, an increasingly effective paradigm is to embed learned modules inside iterative solvers as residual-to-correction maps rather than rely on end-to-end prediction Lerer et al. [2024], Rudikov et al. [2024], Zhang et al. [2024], Cui et al. [2025], Xie et al. [2025], Stanziola et al. [2021]. In its simplest form, a learned operator \mathcal{M}_θ updates $\mathbf{u}^{m+1} = \mathbf{u}^m + \mathcal{M}_\theta(\mathbf{f} - A\mathbf{u}^m)$ and training commonly minimizes an unpreconditioned Euclidean residual mismatch such as $\|A\mathcal{M}_\theta(\mathbf{r}) - \mathbf{r}\|_2$. While this choice is natural, it implicitly fixes a *residual metric* and therefore determines

*Corresponding author.

which spectral components dominate optimization. For indefinite operators, Euclidean residual exhibit particularly stiff landscapes around near-resonant modes Liu et al. [2024], Rahaman et al. [2019], motivating objective designs that reflect the geometry induced by effective preconditioning.

To address this challenge, we observe that the Born Series (integral-equation) and shifted-Laplacian left preconditioning share the same algebraic core. Let $L_\eta := -\Delta - (k_0^2 + i\eta)$ be a damped reference operator, $G_\eta := L_\eta^{-1}$ its inverse, and define $V_\eta := L_\eta - A$ (details in Section 2). Then the identity

$$I - G_\eta V_\eta = G_\eta A = L_\eta^{-1} A$$

shows that the integral residual in Born Series and the shifted-Laplacian left-preconditioned residual are equivalent representations. This equivalence suggests measuring residuals in the preconditioner-induced norm

$$\|\mathbf{r}\|_{R_\eta} := \|G_\eta \mathbf{r}\|_2, \quad R_\eta := G_\eta^* G_\eta,$$

i.e., a Riesz-map metric that inherits the conditioning mechanism of shifted-Laplacian preconditioning.

Guided by these viewpoints, we propose a *Neural Preconditioned Born Series* (NPBS) iteration that generalizes CBS by replacing its scalar correction with a residual-driven neural operator acting in preconditioned coordinates. Related Born-series-inspired works such as the learned Born series (LBS) Stanziola et al. [2023] and the neural Born series operator (NBSO) Zeng et al. [2023] are fixed-depth, CBS-inspired unrolled forward solvers trained to predict Helmholtz wavefields. By contrast, we learn a residual-to-correction map inside an iterative solver. To optimize NPBS, we construct two complementary training objectives from the original system $A\mathbf{u} = \mathbf{f}$ and its left-preconditioned counterpart $G_\eta A\mathbf{u} = G_\eta \mathbf{f}$. Accordingly, we obtain two residual metrics and their associated losses: the Euclidean-metric residual loss $\mathcal{L}_{\text{bs}}^{\ell_2}$ and the preconditioned-metric Born Series-inspired loss $\mathcal{L}_{\text{bs}}^{R_\eta}$ (Section 3.3). We develop our framework primarily based on the Helmholtz equation, and subsequently extend the methodology to other PDE classes, including convection–diffusion–reaction and linearized Newton systems. Our contributions are summarized as follows:

1. **Neural Preconditioned Born Series (NPBS).** We propose NPBS, a learned correction iteration in preconditioned residual coordinates that generalizes the Convergent Born Series (CBS) and is compatible with multiple neural operator architectures.
2. **Residual-metric viewpoint and Born-series-inspired objectives.** Leveraging the identity that connects Born Series residuals with shifted-Laplacian left preconditioning, we derive the preconditioner-induced residual metric $R_\eta = G_\eta^* G_\eta$ and develop two training objectives, $\mathcal{L}_{\text{bs}}^{\ell_2}$ and $\mathcal{L}_{\text{bs}}^{R_\eta}$, with consistent formulations for Helmholtz, CDR, and linearized Newton systems.
3. **Robustness to ill-conditioning and algorithmic generalization.** Experiments demonstrate that the convergence advantage of NPBS over direct baselines widens significantly as the underlying systems become increasingly ill-conditioned (e.g., higher wavenumbers or highly discontinuous media). Furthermore, the methodology generalizes effectively to other PDEs, delivering substantial iteration reductions on convection–diffusion–reaction equations and Newton linearizations of nonlinear problems.

The paper is organized as follows: Section 2 derives the Born/integral equation and establishes its equivalence to shifted-Laplacian left-preconditioning; Section 3.2 introduces NPBS; Section 3.3 presents the Born-series-inspired objectives; and Section 4 reports the experiments.

2 From Born Series to Preconditioned Coordinates

We begin from the classical Born series/Lippmann–Schwinger integral formulation and analyze its algebraic relation to shifted-Laplacian left-preconditioning. The key result (Proposition 2.1) shows that the integral residual and the shifted-Laplacian left-preconditioned residual are mathematically equivalent. This identity motivates both the Neural Preconditioned Born Series (NPBS) solver (Section 3) and the preconditioned training metric (Section 3.3).

2.1 Operator Splitting and Integral Equation

We consider the Helmholtz equation for wave scattering in an unbounded heterogeneous medium, subject to the Sommerfeld radiation condition:

$$\begin{aligned} \mathcal{L}u(x) &:= -\Delta u(x) - k(x)^2 u(x) = f(x), \quad x \in \mathbb{R}^d, \\ \lim_{|x| \rightarrow \infty} |x|^{\frac{d-1}{2}} \left(\frac{\partial u}{\partial |x|} - ik_0 u \right) &= 0, \end{aligned} \tag{1}$$

where u is the wavefield, f the source, d the spatial dimension, and $k(x) = \omega/c(x)$ the spatially varying wavenumber (ω : angular frequency, $c(x)$: speed of sound). The constant k_0 is the background wavenumber ($k(x) \rightarrow k_0$ as $|x| \rightarrow \infty$).

For computation, the unbounded domain is truncated to a bounded domain Ω , and absorbing boundary layers—sponge layers Israeli and Orszag [1981] or PML Berenger [1994], Stanziola et al. [2021]—are incorporated so that the resulting bounded-domain operator (still denoted \mathcal{L}) suppresses spurious reflections. After discretization (finite differences or FFT-based pseudospectral methods), we obtain the linear system

$$A\mathbf{u} = \mathbf{f},$$

where A is the discrete Helmholtz operator (including absorbing-layer terms), \mathbf{u} the discrete unknown, and \mathbf{f} the discrete source. Introduce a damped reference operator

$$\mathcal{L}_\eta := -\Delta - (k_0^2 + i\eta), \quad \eta > 0, \quad (2)$$

used only for preconditioning/training coordinates. The reference is chosen to be transform-diagonalizable (periodic FFT or Dirichlet/Neumann DST/DCT) for fast application; any mismatch between this reference and the physical operator, including absorbing-layer terms, is absorbed into the perturbation

$$\mathcal{V}_\eta := \mathcal{L}_\eta - \mathcal{L}.$$

Let g_η be the Green kernel for the *continuous* reference operator \mathcal{L}_η under the chosen boundary condition on Ω . Define the associated continuous Green operator

$$(\mathcal{G}_\eta q)(x) := \int_{\Omega} g_\eta(x, y) q(y) dy, \quad q \in L^2(\Omega), \quad (3)$$

so that $\mathcal{G}_\eta = \mathcal{L}_\eta^{-1}$ on the admissible function class.

Discrete realization. In the discrete setting, let L_η denote the matrix obtained by discretizing \mathcal{L}_η (e.g., via finite differences or Fourier pseudospectral methods; see Appendix C for details), and define the discrete Green operator $G_\eta := L_\eta^{-1}$. For transform-diagonalizable references (periodic FFT or Dirichlet/Neumann DST/DCT), G_η can be applied in $\mathcal{O}(N \log N)$ operations (Appendix B). For translation-invariant references (free space or periodic box), $g_\eta(x, y) = g_\eta(x - y)$ and (3) reduces to a convolution.

Operator splitting and Lippmann–Schwinger form. With $\mathcal{V}_\eta := \mathcal{L}_\eta - \mathcal{L}$, the heterogeneous Helmholtz operator splits as

$$\mathcal{L} = \mathcal{L}_\eta - \mathcal{V}_\eta. \quad (4)$$

For the coefficient-only Helmholtz split, \mathcal{V}_η reduces to multiplication by $k(x)^2 - k_0^2 - i\eta$.

In the continuous setting, $\mathcal{L}u = f$ implies

$$\mathcal{L}_\eta u = \mathcal{V}_\eta u + f, \quad u = \mathcal{G}_\eta(\mathcal{V}_\eta u + f),$$

equivalently,

$$(\mathcal{I} - \mathcal{G}_\eta \mathcal{V}_\eta)u = \mathcal{G}_\eta f.$$

In the discrete setting, starting from $A\mathbf{u} = \mathbf{f}$ and the discrete split $A = L_\eta - V_\eta$, we obtain

$$(I - G_\eta V_\eta)\mathbf{u} = G_\eta \mathbf{f}. \quad (5)$$

Equation (5) is the preconditioned operator equation used by CBS Osnabrugge et al. [2016]. In translation-invariant settings it coincides with the standard Lippmann–Schwinger form. Solving (5) by fixed-point iteration amounts to a Neumann series in $G_\eta V_\eta$: convergence is guaranteed whenever $\|G_\eta V_\eta\| < 1$, and the rate and conditioning of the preconditioned system are controlled by this norm. This motivates the spectral bounds formalized below.

2.2 Key Identity: Integral Residual = Shifted-Laplacian Left-Preconditioned Residual

Proposition 2.1 (Shifted-preconditioned equivalence and spectral motivation). *Let the discrete Helmholtz operator admit the split $A = L_\eta - V_\eta$, and assume L_η is invertible so that $G_\eta := L_\eta^{-1}$ is well-defined. Then*

$$I - G_\eta V_\eta = G_\eta A = L_\eta^{-1} A. \quad (6)$$

Hence (5) is algebraically identical to the left-preconditioned system

$$L_\eta^{-1} A \mathbf{u} = L_\eta^{-1} \mathbf{f}. \quad (7)$$

Moreover, if $\|G_\eta V_\eta\|_2 \leq \rho < 1$, then

$$\sigma(I - G_\eta V_\eta) \subset \{z \in \mathbb{C} : |z - 1| \leq \rho\}, \quad (8)$$

$$(I - G_\eta V_\eta)^{-1} = \sum_{j=0}^{\infty} (G_\eta V_\eta)^j, \quad (9)$$

and

$$\kappa_2(I - G_\eta V_\eta) \leq \frac{1 + \rho}{1 - \rho}. \quad (10)$$

Proof. Using $A = L_\eta - V_\eta$ and $G_\eta L_\eta = I$:

$$I - G_\eta V_\eta = G_\eta L_\eta - G_\eta V_\eta = G_\eta(L_\eta - V_\eta) = G_\eta A.$$

For the spectral part, $\rho(G_\eta V_\eta) \leq \|G_\eta V_\eta\|_2 \leq \rho$ implies each eigenvalue μ of $G_\eta V_\eta$ satisfies $|\mu| \leq \rho$. Therefore eigenvalues of $I - G_\eta V_\eta$ are $1 - \mu$, which yields (8). Since $\|G_\eta V_\eta\|_2 < 1$, the Neumann series (9) converges. Also

$$\|I - G_\eta V_\eta\|_2 \leq 1 + \rho, \quad \|(I - G_\eta V_\eta)^{-1}\|_2 \leq \sum_{j \geq 0} \rho^j = \frac{1}{1 - \rho},$$

which implies (10). \square

2.3 CBS as Richardson Iteration in Preconditioned Coordinates

The CBS fixed-point iteration Osnabrugge et al. [2016] is

$$\mathbf{u}^{m+1} = \mathbf{u}^m + \gamma(G_\eta(V_\eta \mathbf{u}^m + \mathbf{f}) - \mathbf{u}^m), \quad (11)$$

where γ is a scalar/diagonal relaxation. By (6):

$$\mathbf{u}^{m+1} = \mathbf{u}^m + \gamma G_\eta(\mathbf{f} - A\mathbf{u}^m), \quad (12)$$

which is Richardson iteration preconditioned by the shifted Laplacian L_η . Thus CBS, usually derived from integral-equation theory, is equivalently the simplest left-preconditioned stationary method in the differential-operator framework. The scalar γ limits the correction to a single-parameter family; replacing it with a richer correction map is the subject of the next section.

Role of η in metric and iteration coordinates. The shift η defines both the left preconditioner $G_\eta := L_\eta^{-1}$ and the induced residual metric $R_\eta := G_\eta^* G_\eta$. Consequently, the R_η -weighted residual norm satisfies

$$\|\mathbf{f} - A\mathbf{u}\|_{R_\eta}^2 := (\mathbf{f} - A\mathbf{u})^* R_\eta (\mathbf{f} - A\mathbf{u}) = \|G_\eta(\mathbf{f} - A\mathbf{u})\|_2^2,$$

so η controls the geometry in which residuals are measured and corrected, not only numerical damping. In practice, we tune η via a small validation sweep and then keep it fixed between training and inference for each dataset to preserve objective–inference consistency. Increasing η often decreases $\|G_\eta V_\eta\|$ and improves the contraction of fixed-point iterations, whereas overly large η can over-damp informative corrections.

3 Neural Preconditioned Born Series Method

3.1 Direct-residual neural iteration and training loss

A common learned linear-solver baseline uses a neural correction map \mathcal{M}_θ driven by the *unpreconditioned* residual. Given the discrete system $A\mathbf{u} = \mathbf{f}$, define the residual $\mathbf{r}^m := \mathbf{f} - A\mathbf{u}^m$ and iterate

$$\mathbf{u}^{m+1} = \mathbf{u}^m + \mathcal{M}_\theta(\mathbf{r}^m) = \mathbf{u}^m + \mathcal{M}_\theta(\mathbf{f} - A\mathbf{u}^m), \quad (13)$$

which operates in Euclidean residual coordinates.

A standard training objective for \mathcal{M}_θ is to minimize the relative residual of the learned inverse action on random probes. Let \mathcal{D} denote a probe/residual distribution (e.g., $\mathcal{N}(0, I)$ or residual-replay samples). Then:

$$\mathcal{L}_{\text{dir}}(\theta) = \mathbb{E}_{\mathbf{r} \sim \mathcal{D}} \frac{\|A\mathcal{M}_\theta(\mathbf{r}) - \mathbf{r}\|_2}{\|\mathbf{r}\|_2}. \quad (14)$$

This objective is simple and widely used Cui et al. [2025], Xie et al. [2025], but it optimizes the residual in *unpreconditioned* Euclidean geometry; for indefinite Helmholtz operators, near-resonant modes can yield stiff gradients and slow learning.

3.2 Neural Preconditioned Born Series (NPBS) iteration

Proposition 2.1 shows that the Lippmann–Schwinger/CBS operator corresponds to left preconditioning by the shifted Laplacian. CBS uses a scalar relaxation γ in these preconditioned coordinates; NPBS replaces γI with a learned operator \mathcal{M}_θ acting in the *same* coordinates.

Efficient integral-form implementation. Define the Born fixed-point map $\mathbf{u} \mapsto G_\eta(V_\eta \mathbf{u} + \mathbf{f})$. At iterate u^m , NPBS updates via

$$\mathbf{u}^{m+1} = \mathbf{u}^m + \mathcal{M}_\theta(G_\eta(V_\eta \mathbf{u}^m + \mathbf{f}) - \mathbf{u}^m). \quad (15)$$

Here $V_\eta \mathbf{u}^m$ is pointwise multiplication and G_η is applied once (e.g., via FFT for transform-diagonalizable references), so each iteration requires only a single transform pair for the preconditioned residual. If $\mathcal{M}_\theta = \gamma I$, (15) reduces to CBS (cf. (11)). If $\mathcal{M}_\theta = (I - G_\eta V_\eta)^{-1}$, then one NPBS step recovers the exact Helmholtz solution.

Equivalent left-preconditioned (differential) form. Using the key identity (6), (15) is equivalently

$$\mathbf{u}^{m+1} = \mathbf{u}^m + \mathcal{M}_\theta(G_\eta(\mathbf{f} - A\mathbf{u}^m)), \quad (16)$$

which makes the left-preconditioned interpretation explicit: the network input is $\mathbf{r}_{\text{bs}}^m := G_\eta(\mathbf{f} - A\mathbf{u}^m) = L_\eta^{-1}(\mathbf{f} - A\mathbf{u}^m)$. Computing $A\mathbf{u}^m$ may require an additional application of the discrete Laplacian (e.g., an extra FFT in pseudospectral settings), hence we implement the efficient integral form (15) in practice. Proposition 2.1 implies that the preconditioned coordinates enjoy spectral clustering when $\|G_\eta V_\eta\| < 1$, justifying their use for both iteration and training.

3.3 Born-series-inspired loss as a preconditioned residual metric

We begin by analyzing the operator targets implied by the training objectives. The direct loss (14) trains \mathcal{M}_θ to approximate A^{-1} in unpreconditioned coordinates. In contrast, the NPBS iteration (15) evaluates the network in preconditioned coordinates. Here, the effective target is $\mathcal{M}_\theta \approx (I - G_\eta V_\eta)^{-1}$ (or equivalently, $\mathcal{M}_\theta \approx (G_\eta A)^{-1}$ via (6)). Consequently, a model trained exclusively with (14) lacks alignment with the NPBS operator structure.

To resolve this misalignment, an intermediate approach views the composition $\mathcal{M}_\theta G_\eta$ as an approximation of A^{-1} . Adopting this within the standard residual training paradigm (14) yields

$$\mathcal{L}_{\text{bs}}^{\ell_2}(\theta) = \mathbb{E}_{\mathbf{r} \sim \mathcal{D}} \frac{\|A\mathcal{M}_\theta(G_\eta \mathbf{r}) - \mathbf{r}\|_2}{\|\mathbf{r}\|_2}. \quad (17)$$

Although (17) successfully evaluates the network on the preconditioned inputs $G_\eta \mathbf{r}$, it measures the residual in the original Euclidean geometry associated with $A\mathbf{u} = \mathbf{f}$. Thus, it fails to capture the residual geometry of the left-preconditioned system $G_\eta A\mathbf{u} = G_\eta \mathbf{f}$. Measuring the residual after left preconditioning, and incorporating the identity (6), we propose the full Born Series-inspired objective:

$$\mathcal{L}_{\text{bs}}^{R_\eta}(\theta) = \mathbb{E}_{\mathbf{r} \sim \mathcal{D}} \frac{\|(I - G_\eta V_\eta)\mathcal{M}_\theta(G_\eta \mathbf{r}) - G_\eta \mathbf{r}\|_2}{\|G_\eta \mathbf{r}\|_2}. \quad (18)$$

In (18), we represent the preconditioned operator as $I - G_\eta V_\eta$ rather than $G_\eta A$. This computationally efficient form requires only a single transform application, mirroring the practical implementation of the NPBS iteration (15). Unlike (17), this proposed objective thoroughly aligns both the input representation and the residual metric with the underlying preconditioned system.

Proposition 3.1 (Riesz-map equivalence). *Define*

$$R_\eta := G_\eta^* G_\eta, \quad \|\mathbf{x}\|_{R_\eta} := \|G_\eta \mathbf{x}\|_2, \quad \langle \mathbf{x}, \mathbf{y} \rangle_{R_\eta} := \langle \mathbf{x}, R_\eta \mathbf{y} \rangle_2.$$

Then (18) is equivalently

$$\mathcal{L}_{\text{bs}}^{R_\eta}(\theta) = \mathbb{E}_{\mathbf{r} \sim \mathcal{D}} \frac{\|A\mathcal{M}_\theta(G_\eta \mathbf{r}) - \mathbf{r}\|_{R_\eta}}{\|\mathbf{r}\|_{R_\eta}}. \quad (19)$$

Proof. Using (6), (18) can be rewritten as

$$\mathcal{L}_{\text{bs}}^{R_\eta}(\theta) = \mathbb{E}_{\mathbf{r} \sim \mathcal{D}} \frac{\|G_\eta A \mathcal{M}_\theta(G_\eta \mathbf{r}) - G_\eta \mathbf{r}\|_2}{\|G_\eta \mathbf{r}\|_2}. \quad (20)$$

By definition, $\|\mathbf{x}\|_{R_\eta} = \|G_\eta \mathbf{x}\|_2$. Substituting $\mathbf{x} = A\mathcal{M}_\theta(G_\eta \mathbf{r}) - \mathbf{r}$ gives $\|A\mathcal{M}_\theta(G_\eta \mathbf{r}) - \mathbf{r}\|_{R_\eta} = \|G_\eta A \mathcal{M}_\theta(G_\eta \mathbf{r}) - G_\eta \mathbf{r}\|_2$, and similarly $\|\mathbf{r}\|_{R_\eta} = \|G_\eta \mathbf{r}\|_2$, yielding (19). \square

Proposition 3.1 makes precise that (18) and (19) are the same objective written in two equivalent forms. It also clarifies the relation between the bridge loss and the fully preconditioned loss: $\mathcal{L}_{\text{bs}}^{\ell_2}$ in (17) and $\mathcal{L}_{\text{bs}}^{R_\eta}$ in (19) use the same NPBS-compatible input $G_\eta \mathbf{r}$ and the same residual of the original operator, $A\mathcal{M}_\theta(G_\eta \mathbf{r}) - \mathbf{r}$, but evaluate that residual in different norms (Euclidean versus R_η -induced). Thus, relative to (14), the progression is: unpreconditioned probes with Euclidean norm (\mathcal{L}_{dir}), then preconditioned probes with Euclidean norm ($\mathcal{L}_{\text{bs}}^{\ell_2}$), and finally preconditioned probes with the R_η -metric ($\mathcal{L}_{\text{bs}}^{R_\eta}$).

Why this mitigates training difficulty. Relative to (14), (17) and (18) replace the direct regression target A^{-1} with the preconditioned target $(G_\eta A)^{-1}$ by feeding $G_\eta \mathbf{r}$ into \mathcal{M}_θ . The key difference lies in the residual metric: $\mathcal{L}_{\text{bs}}^{\ell_2}$ measures the physical residual $e(\mathbf{r}; \theta) := A\mathcal{M}_\theta(G_\eta \mathbf{r}) - \mathbf{r}$ in the Euclidean norm $\|e(\mathbf{r}; \theta)\|_2$, whereas $\mathcal{L}_{\text{bs}}^{R_\eta}$ measures it in the preconditioned norm $\|e(\mathbf{r}; \theta)\|_{R_\eta} = \|G_\eta e(\mathbf{r}; \theta)\|_2$. By Proposition 3.1, this aligns training gradients with the preconditioned coordinates used by NPBS inference. For the constant-coefficient Helmholtz reference, the Fourier symbol

$$\widehat{G}_\eta(\boldsymbol{\xi}) = \frac{1}{|\boldsymbol{\xi}|^2 - k_0^2 - i\eta}$$

shows explicitly how the metric reweights residual modes in an η -controlled way. The practical benefit is that optimization is performed in the left preconditioned coordinates of $G_\eta A = I - G_\eta V_\eta$. When $\|G_\eta V_\eta\| < 1$ (Proposition 2.1), the spectrum of $G_\eta A$ is concentrated near 1, so different modal components are brought to a more comparable scale. This reduces anisotropy/stiffness of the operator target relative to training directly against A , which in turn improves optimization stability.

Remark 3.2 (Training/inference consistency). At inference, the NPBS network input is the Born residual

$$\mathbf{r}_{\text{bs}}^m = G_\eta(\mathbf{f} - A\mathbf{u}^m). \quad (21)$$

The training inputs in (17) and (18) have the same form $G_\eta \mathbf{r}$. Exact distribution matching holds if \mathcal{D} is chosen as the empirical distribution of iterative residuals (e.g., rollout replay). To mitigate the overhead of dataset preparation, we enforce form-level alignment and treat residual-replay matching as an optional refinement. Implementation follows directly from the definitions above: (i) fix η and the reference operator L_η (hence G_η), (ii) train \mathcal{M}_θ by sampling $\mathbf{r} \sim \mathcal{D}$ and minimizing (18) (or (20)), and (iii) at inference iterate (15) until $\|\mathbf{f} - A\mathbf{u}^m\|_2 / \|\mathbf{f}\|_2 \leq \text{rTol}$ (see the definition in (22)).

The derivation and operator identities for the Helmholtz setting are presented in the main text. For completeness and to highlight broader applicability, the corresponding derivations for the CDR equation and for linearized Newton systems arising from nonlinear PDEs are deferred to Appendix A. Fast-application verification of the Green operators (including Proposition B.1) is provided in Appendix B, and the Fourier pseudospectral discretization recipe is summarized in Appendix C. Finally, while the present work *does not focus on network architecture design*, the specific architectures used in our experiments are documented in Appendix D.

4 Numerical Results

We evaluate the proposed framework along two orthogonal design axes: (i) *iteration format and training objective*, contrasting the direct iteration (using \mathcal{L}_{dir}) with the NPBS iteration (using $\mathcal{L}_{\text{bs}}^{\ell_2}$ and $\mathcal{L}_{\text{bs}}^{R_\eta}$); and (ii) *solver architecture*, comparing the classical scalar-corrected CBS against the learned NPBS framework instantiated by PA-FNO (detailed in Appendix D). We primarily benchmark our method on the Helmholtz equation. To demonstrate the generality of the NPBS framework and its loss-design principles, we further extend our evaluation to convection-diffusion-reaction (CDR) equations and linearized Newton systems for nonlinear PDEs. Across all PDE settings, models were trained independently from scratch.

For reproducibility, all experiments were conducted using PyTorch 2.6.0 with CUDA 12.4 on a workstation equipped with an Intel Xeon Platinum 8468 CPU and a single NVIDIA H100 GPU. Unless otherwise noted, reported metrics represent the average across 50 test samples. We employed a unified stopping criterion,

$$\text{rTol} = \frac{\|\mathbf{f} - A\mathbf{u}^m\|_2}{\|\mathbf{f}\|_2}, \quad (22)$$

for all methods and datasets so that iteration counts are directly comparable. The PA-FNO neural operator utilizes a network architecture consisting of 3 stacked layers, 25 hidden channels, and 45 Fourier modes for NLFL. During the training phase, the networks are optimized over 400 epochs using an initial learning rate of 5×10^{-4} , which is subsequently modulated by a step learning rate scheduler.

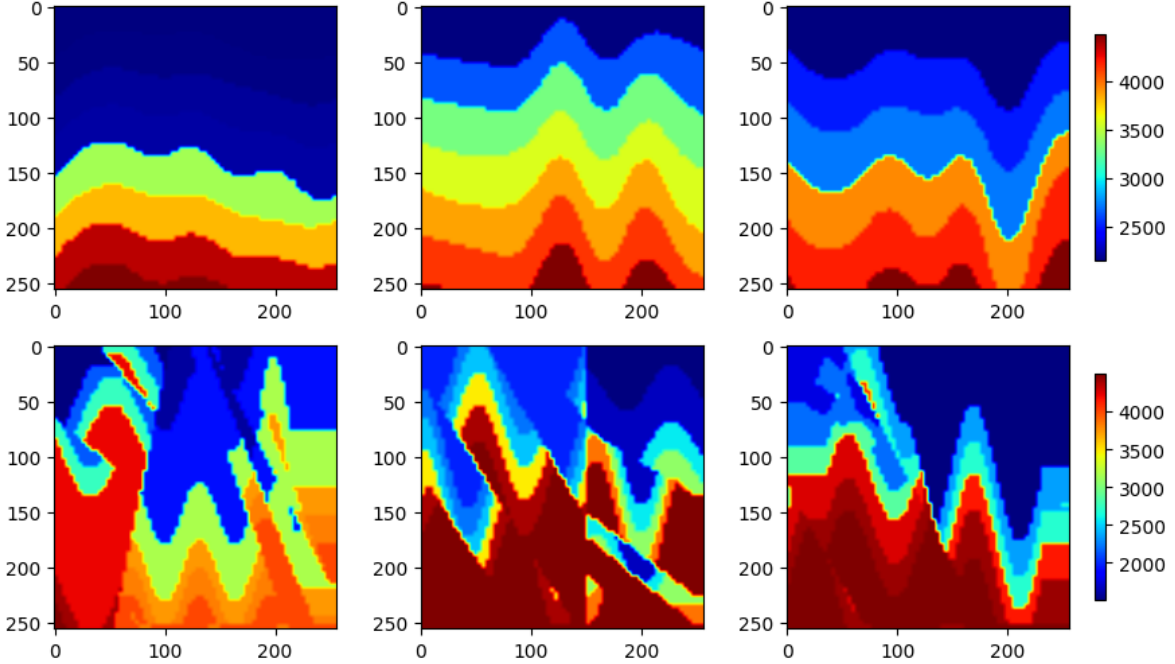


Figure 1: Representative heterogeneous velocity models from the OpenFWI datasets. Top row: CurveVel-A, featuring relatively smooth, curved velocity transitions. Bottom row: CurveFault-B, characterized by sharp discontinuities, strong contrasts, and complex fault structures.

4.1 Heterogeneous Helmholtz Equation

For the heterogeneous Helmholtz equation, we select two distinct datasets from OpenFWI Deng et al. [2022] to systematically evaluate our method across progressive difficulty levels: CurveVel-A and CurveFault-B (illustrated in Figure 1). CurveVel-A introduces intermediate complexity with relatively smooth, curved velocity profiles. In contrast, CurveFault-B presents a highly challenging target characterized by strong heterogeneity, sharp velocity contrasts, and severe structural discontinuities (faults). By comparing convergence behaviors across this hierarchy of complexity, we demonstrate that the advantages of our proposed NPBS framework become increasingly pronounced as the underlying physical problem becomes more ill-conditioned and challenging.

In our experimental setup, spatial velocity fields range from approximately 1500 to 4500 m/s and are discretized onto a 256×256 grid. To simulate infinite boundary conditions, perfectly matched layers (PML) consisting of 32 grid points are applied to the domain margins. We dictate the grid resolution such that there are at least 12 points per wavelength (ppw).

4.1.1 Iteration format and loss comparison

We isolate the effect of the network iteration format and the choice of training loss on solver efficiency. The evaluation compares three configurations under a unified stopping rule ($rTol = 10^{-6}$): (i) Direct iteration trained with \mathcal{L}_{dir} , (ii) NPBS iteration trained with $\mathcal{L}_{\text{bs}}^{\ell_2}$, and (iii) NPBS iteration trained with the physics-aligned $\mathcal{L}_{\text{bs}}^{R_\eta}$. Because all models must satisfy the same strict physical residual tolerance, the required iterations provide an unambiguous measure of how effectively each formulation conditions the heterogeneous Helmholtz problem.

Table 1 reports the effect of iteration scheme and training loss on two OpenFWI datasets with increasing difficulty. NPBS + $\mathcal{L}_{\text{bs}}^{R_\eta}$ achieves the fewest iterations on both datasets, and both NPBS variants outperform Direct + \mathcal{L}_{dir} . Notably, the gain of NPBS + $\mathcal{L}_{\text{bs}}^{R_\eta}$ over the direct baseline increases from $1.6\times$ on CurveVel-A to $2.0\times$ on CurveFault-B, suggesting that the metric-matched objective becomes more beneficial as the medium becomes more heterogeneous and ill-conditioned.

Table 2 shows the trend as ppw decreases from 24 to 12, which corresponds to increasing effective wavenumber and a harder Helmholtz regime. Although all methods require more iterations at higher wavenumbers, NPBS + $\mathcal{L}_{\text{bs}}^{R_\eta}$ remains

Table 1: Iteration format and loss comparison across OpenFWI datasets of increasing difficulty ($rTol = 10^{-6}$). Ratio provides the comparison of $NPBS + \mathcal{L}_{bs}^{R_\eta}$ against $Direct + \mathcal{L}_{dir}$.

Dataset	Average Iterations			Ratio
	Direct + \mathcal{L}_{dir}	NPBS + $\mathcal{L}_{bs}^{\ell_2}$	NPBS + $\mathcal{L}_{bs}^{R_\eta}$	
CurveVel-A	491	466	300	1.6
CurveFault-B	1150	689	561	2.0

Table 2: Wavenumber-dependent performance on CurveFault-B (lower ppw corresponds to higher wavenumber) under $rTol = 10^{-6}$. Ratio provides the comparison of $NPBS + \mathcal{L}_{bs}^{R_\eta}$ against $Direct + \mathcal{L}_{dir}$.

ppw	Average Iterations			Ratio
	Direct + \mathcal{L}_{dir}	NPBS + $\mathcal{L}_{bs}^{\ell_2}$	NPBS + $\mathcal{L}_{bs}^{R_\eta}$	
24	471	514	392	1.2
20	611	564	438	1.4
16	708	683	475	1.5
12	1150	689	561	2.0

consistently best, and its speedup over $Direct + \mathcal{L}_{dir}$ increases from $1.2\times$ to $2.0\times$. This confirms that the proposed metric-matched formulation yields larger gains as the wavenumber (and problem difficulty) increases.

4.1.2 Architecture effect: learned NPBS solver vs classical CBS

Table 3 compares classical CBS (scalar update) and NPBS (learned update) under the same stopping rule. At both $rTol = 10^{-4}$ and $rTol = 10^{-6}$, NPBS requires fewer iterations than CBS on both datasets. This indicates that learned preconditioning has strong potential to reduce iteration count. Figure 2 depicts a representative sample from the OpenFWI CurveFault-B dataset alongside the corresponding wavefield and convergence profiles.

Table 3: Architecture-level comparison of CBS and learned NPBS on OpenFWI datasets.

Dataset	$rTol = 10^{-4}$		$rTol = 10^{-6}$	
	CBS Iters	NPBS Iters	CBS Iters	NPBS Iters
CurveVel-A	402	166	1014	300
CurveFault-B	533	415	1124	561

However, iteration reduction alone does not imply end-to-end runtime gains. Wall-clock efficiency additionally depends on careful architecture and systems design (e.g., model size, operator efficiency, and memory-compute balance), which is beyond the scope of this work.

4.2 Algorithmic Generalization Beyond the Helmholtz Equation

4.2.1 Linear Convection-Diffusion-Reaction (CDR) Systems

For the linear CDR equation

$$-\nabla \cdot (\kappa \nabla u) + \mathbf{v} \cdot \nabla u + \sigma u = f \quad \text{in } \Omega \subset \mathbb{R}^d, \quad (23)$$

subject to periodic boundary conditions, we employ the PA-FNO architecture (Eq. (43)) as the neural preconditioner \mathcal{M}_θ . The primary objective of this evaluation is to investigate whether the algorithmic and loss-design findings established for the Helmholtz equation generalize to the CDR equation. Consequently, this study maintains a fixed neural architecture to focus exclusively on comparing iteration formulations and training objectives. Specifically, we evaluate the direct solution approach ($Direct + \mathcal{L}_{dir}$) against the neural preconditioned basic stationary iterations trained with either standard L_2 loss ($NPBS + \mathcal{L}_{bs}^{\ell_2}$) or our proposed residual-based relative loss ($NPBS + \mathcal{L}_{bs}^{R_\eta}$).

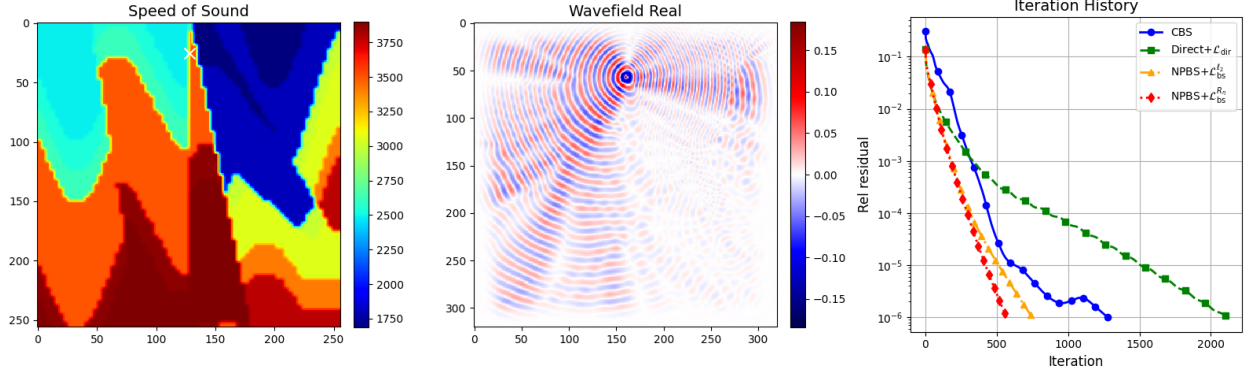


Figure 2: Iteration comparison of different strategies on a representative instance from the OpenFWI CurveFault-B dataset.

To isolate these effects, we construct a synthetic dataset on a 128×128 periodic grid with heterogeneous diffusion κ , velocity \mathbf{v} , and reaction rate σ . We sample κ from a Gaussian random field (GRF). To enforce incompressibility ($\nabla \cdot \mathbf{v} = 0$), we generate \mathbf{v} from a GRF stream function ψ as

$$v_x = \frac{\partial \psi}{\partial y}, \quad v_y = -\frac{\partial \psi}{\partial x}.$$

The source term f is a Gaussian bump with random center and width. Representative samples are shown in Figure 3. We keep the network architecture and training hyperparameters the same as in Section 4.

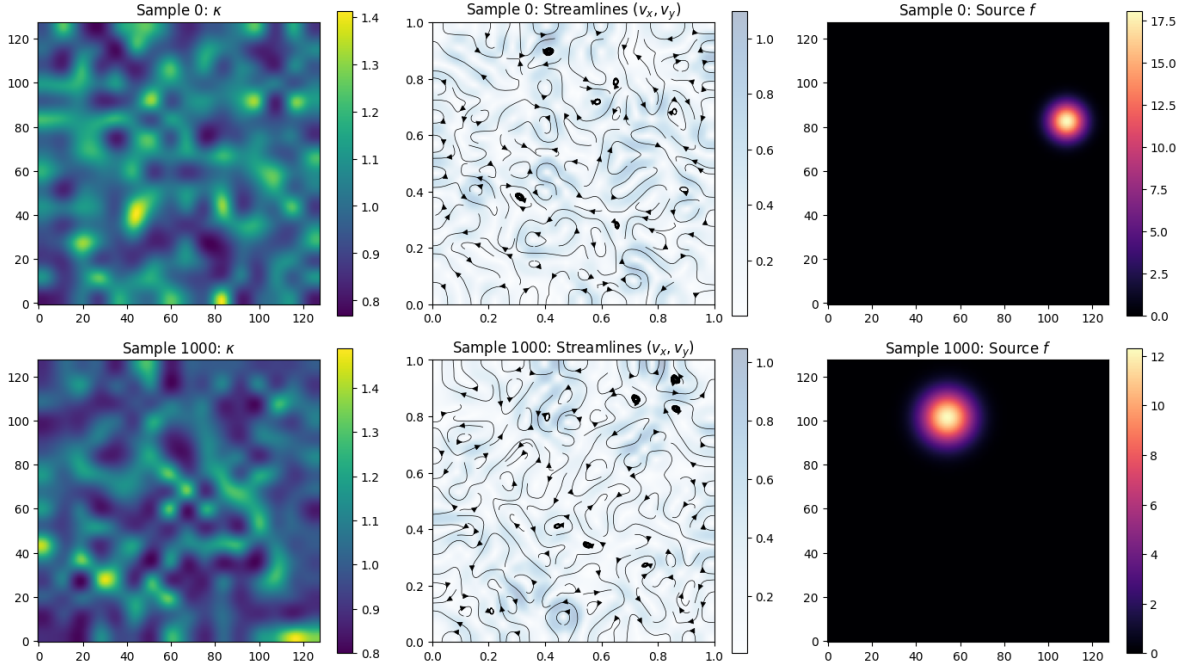
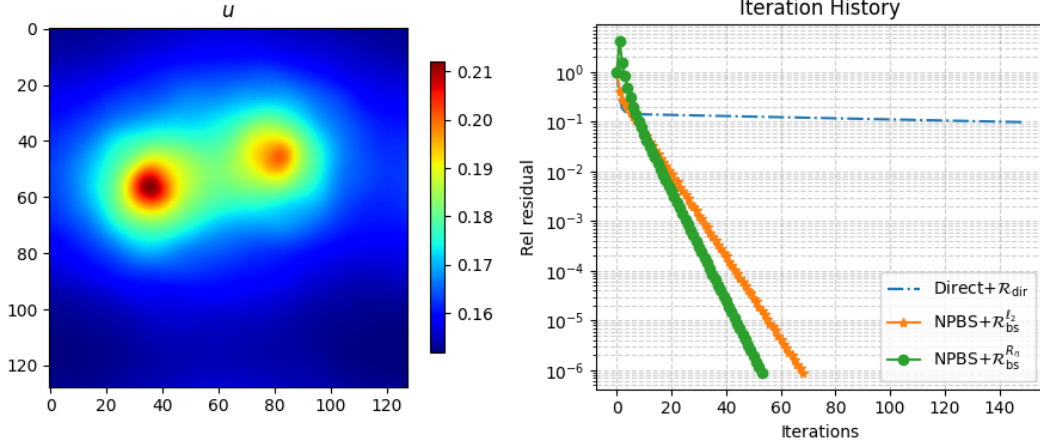


Figure 3: CDR dataset samples: diffusion κ , velocity field \mathbf{v} , and source term f .

Table 4 reports the CDR transfer performance under matched rTol (22). The results demonstrate that the NPBS framework generalizes effectively to convection–diffusion–reaction equations. Specifically, NPBS+ $\mathcal{L}_{\text{bs}}^{R_n}$ achieves the fastest convergence with 59 iterations on average, followed by NPBS+ $\mathcal{L}_{\text{bs}}^{\ell_2}$ with 66 iterations. Both represent a massive improvement over the Direct+ \mathcal{L}_{dir} baseline, which requires over 4500 iterations. This indicates that even for simpler transport-type equations, measuring residuals in preconditioned coordinates during training significantly enhances the solver’s correction ability. Representative residual histories are provided in Figure 4.

Method (iteration + loss)	Avg. Iters	Avg. Rel Res
Direct + \mathcal{L}_{dir}	4533	9.98×10^{-7}
NPBS + $\mathcal{L}_{\text{bs}}^{\ell_2}$	66	9.31×10^{-7}
NPBS + $\mathcal{L}_{\text{bs}}^{R_\eta}$	59	8.89×10^{-7}

Table 4: CDR transfer comparison: iteration count and final relative residual under matched stopping criterion.

Figure 4: CDR residual histories on the synthetic dataset: Direct+ \mathcal{L}_{dir} versus NPBS+ $\mathcal{L}_{\text{bs}}^{\ell_2}$ and NPBS+ $\mathcal{L}_{\text{bs}}^{R_\eta}$.

4.2.2 Linearized Newton systems for nonlinear PDEs

As a nonlinear benchmark, we consider the non-convex problem with multiple solutions from Hao et al. [2024]:

$$\begin{cases} -\Delta u(x, y) - u(x, y)^2 = -s \sin(\pi x) \sin(\pi y), & (x, y) \in \Omega, \\ u(x, y) = 0, & (x, y) \in \partial\Omega, \end{cases} \quad (24)$$

with $f(x, y) := -s \sin(\pi x) \sin(\pi y)$ and nonlinear residual

$$\mathcal{F}_{\text{nl}}(u) := -\Delta u - u^2 - f.$$

At Newton iterate $u^{(m)}$, we solve

$$\begin{cases} -\Delta(\delta u^{(m)}) - 2u^{(m)} \delta u^{(m)} = -\mathcal{F}_{\text{nl}}(u^{(m)}), & (x, y) \in \Omega, \\ \delta u^{(m)} = 0, & (x, y) \in \partial\Omega. \end{cases} \quad (25)$$

and update $u^{(m+1)} = u^{(m)} + \delta u^{(m)}$. In each Newton step, the learned preconditioner is applied to the inner linear system in Eq. (25), and we again evaluate transfer of iteration format/loss design (Direct+ \mathcal{L}_{dir} vs NPBS+ $\mathcal{L}_{\text{bs}}^{\ell_2}$ and NPBS+ $\mathcal{L}_{\text{bs}}^{R_\eta}$), without introducing a separate solver-architecture comparison in this subsection.

In our experiments, we use $\Omega = [0, 1]^2$ with homogeneous Dirichlet boundary conditions and $s = 1600$, following the setup in Hao et al. [2024]. The Laplacian is discretized by a 5-point finite-difference stencil on $N = 63$ interior points, so the Jacobian is $J(u) = (-\Delta) - 2u$. Newton trajectories are generated with sparse direct solves and used as supervision. Initial guesses are perturbed from a reference solution via low-frequency sine-series noise:

$$u^0 = u^* + \alpha \sum_{i,j=1}^4 c_{ij} \sin(i\pi x) \sin(j\pi y), \quad c_{ij} \sim \mathcal{N}(0, 0.1^2), \quad \alpha = 4.0.$$

Figure 5 shows representative solution branches from different initial guesses. The network architecture and training hyperparameters are kept consistent with the configuration detailed in Section 4.

Figure 6 and Fig. 7 illustrate the accelerated inner-loop residual reduction when NPBS-based kernels are embedded within the Newton framework. Quantitative results are summarized in Table 5. Interestingly, for these Newton Jacobian

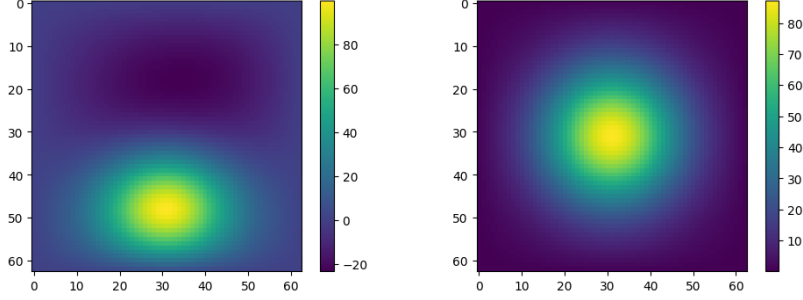
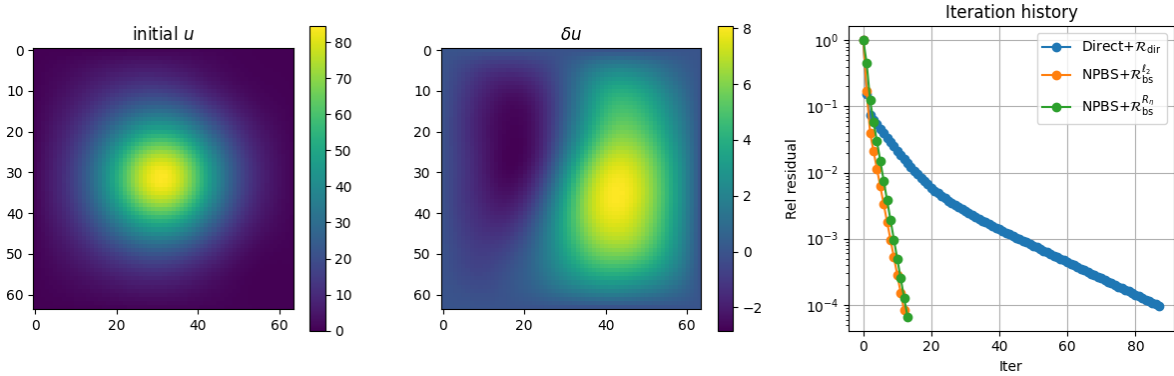
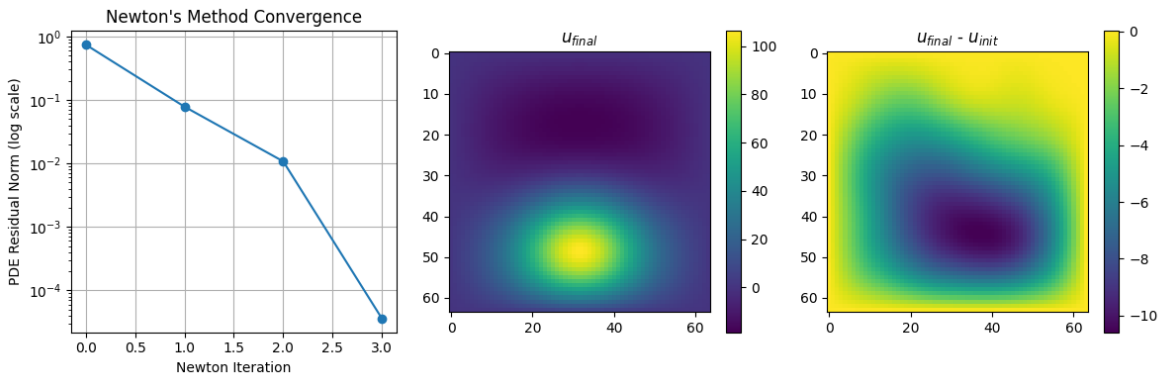


Figure 5: Multiple solutions of the nonlinear PDE under different initial guesses.

systems, $\text{NPBS}+\mathcal{L}_{\text{bs}}^{\ell_2}$ slightly outperforms $\text{NPBS}+\mathcal{L}_{\text{bs}}^{R_\eta}$. This is likely because the linearized systems in this specific nonlinear setup are relatively well-conditioned compared to high-frequency Helmholtz. Since $\mathcal{L}_{\text{bs}}^{\ell_2}$ targets the Euclidean residual of the original system ($Au = f$) directly in preconditioned coordinates, it can achieve superior efficiency in regimes where the extreme spectral rescaling of the R_η metric is not strictly required. Nevertheless, both NPBS variants reduce iteration counts by over $4\times$ compared to the $\text{Direct}+\mathcal{L}_{\text{dir}}$ approach.

Figure 6: Linearized Newton systems inference comparison: $\text{Direct}+\mathcal{L}_{\text{dir}}$ versus $\text{NPBS}+\mathcal{L}_{\text{bs}}^{\ell_2}$ and $\text{NPBS}+\mathcal{L}_{\text{bs}}^{R_\eta}$.Figure 7: PA-FNO preconditioner with $\text{NPBS}+\mathcal{L}_{\text{bs}}^{R_\eta}$ embedded in Newton iterations.

5 Conclusion

This study establishes that designing training objectives for learned PDE preconditioners is fundamentally a metric-selection problem. By linking the convergent Born series with shifted-Laplacian preconditioning, we derived a

Method (iteration + loss)	Avg. Iters	Avg. Rel Res
Direct + \mathcal{L}_{dir}	58	9.52×10^{-5}
NPBS + $\mathcal{L}_{\text{bs}}^{\ell_2}$	12	5.78×10^{-5}
NPBS + $\mathcal{L}_{\text{bs}}^{R_\eta}$	13	6.39×10^{-5}

Table 5: Newton inner-loop iteration comparison under matched stopping criterion.

principled Riesz-map metric ($R_\eta = G_\eta^* G_\eta$) that aligns the training landscape with inference geometry. Building on this, we introduced the Neural Preconditioned Born Series (NPBS) iteration paired with a metric-matched loss ($\mathcal{L}_{\text{bs}}^{R_\eta}$). This approach replaces traditional scalar corrections with a residual-driven neural operator, successfully inheriting the spectral benefits of classical preconditioning while retaining computational efficiency. Evaluations across heterogeneous Helmholtz, convection-diffusion-reaction, and linearized Newton systems highlight two orthogonal performance gains. At the solver level, learned neural operators drastically reduce iteration counts compared to classical methods. At the objective level, optimizing within the preconditioned metric proves essential for indefinite, high-contrast systems where Euclidean losses are difficult to optimize, though the simpler coordinate-matched Euclidean loss ($\mathcal{L}_{\text{bs}}^{\ell_2}$) suffices for relatively well-conditioned scenarios.

While the NPBS framework provides a robust and theoretically grounded approach, it also highlights a current limitation of learning-based preconditioners: although they demonstrate a significant advantage over traditional methods in reducing iteration counts, they still fall short in total computational wall-clock time due to the heavy inference overhead of neural networks. Therefore, to fully realize the practical potential of these methods and solve the time bottleneck, future work must prioritize the design of highly computationally efficient neural preconditioner architectures. Furthermore, extending this metric-driven framework to three-dimensional problems, time-dependent evolution equations, and multi-physics applications remains a promising direction for future research.

References

- Ivo Babuška and Stefan A Sauter. Is the pollution effect of the fem avoidable for the helmholtz equation considering high wave numbers? *SIAM Journal on Numerical Analysis*, 34(6):2392–2423, 1997.
- Christiaan C Stolk. A dispersion minimizing scheme for the 3-d helmholtz equation based on ray theory. *Journal of Computational Physics*, 314:618–646, 2016.
- Oliver G Ernst and Martin J Gander. Why it is difficult to solve helmholtz problems with classical iterative methods. *Numerical analysis of multiscale problems*, pages 325–363, 2011.
- Yogi A Erlangga, Cornelis Vuik, and Cornelis Willebrordus Oosterlee. On a class of preconditioners for solving the helmholtz equation. *Applied Numerical Mathematics*, 50(3-4):409–425, 2004.
- Achi Brandt and Irene Livshits. Wave-ray multigrid method for standing wave equations. *Electronic Transactions on Numerical Analysis*, 6:162–181, 1997.
- Irene Livshits and Achi Brandt. Accuracy properties of the wave-ray multigrid algorithm for helmholtz equations. *SIAM Journal on Scientific Computing*, 28(4):1228–1251, 2006.
- Gerwin Osnabrugge, Saroch Leedumrongwathanakun, and Ivo M Vellekoop. A convergent born series for solving the inhomogeneous helmholtz equation in arbitrarily large media. *Journal of computational physics*, 322:113–124, 2016.
- Zhiming Chen and Xueshuang Xiang. A source transfer domain decomposition method for helmholtz equations in unbounded domain. *SIAM Journal on Numerical Analysis*, 51(4):2331–2356, 2013.
- Wei Leng and Lili Ju. Trace transfer-based diagonal sweeping domain decomposition method for the helmholtz equation: Algorithms and convergence analysis. *Journal of Computational Physics*, 455:110980, 2022.
- Maziar Raissi, Paris Perdikaris, and George E Karniadakis. Physics-informed neural networks: A deep learning framework for solving forward and inverse problems involving nonlinear partial differential equations. *Journal of Computational physics*, 378:686–707, 2019.
- Kamyar Azzadenesheli, Nikola Kovachki, Zongyi Li, Miguel Liu-Schiaffini, Jean Kossaifi, and Anima Anandkumar. Neural operators for accelerating scientific simulations and design. *Nature Reviews Physics*, pages 1–9, 2024.
- Lu Lu, Pengzhan Jin, Guofei Pang, Zhongqiang Zhang, and George Em Karniadakis. Learning nonlinear operators via deeponet based on the universal approximation theorem of operators. *Nature machine intelligence*, 3(3):218–229, 2021.

- Zongyi Li, Nikola Kovachki, Kamyar Azizzadenesheli, Burigede Liu, Kaushik Bhattacharya, Andrew Stuart, and Anima Anandkumar. Fourier neural operator for parametric partial differential equations. *arXiv preprint arXiv:2010.08895*, 2020.
- Zongyi Li, Daniel Zhengyu Huang, Burigede Liu, and Anima Anandkumar. Fourier neural operator with learned deformations for pdes on general geometries. *arXiv preprint arXiv:2207.05209*, 2022.
- Md Ashiqur Rahman, Zachary E Ross, and Kamyar Azizzadenesheli. U-no: U-shaped neural operators. *arXiv e-prints*, pages arXiv–2204, 2022.
- Juncai He, Xinliang Liu, and Jinchao Xu. Mgno: Efficient parameterization of linear operators via multigrid. In *International Conference on Learning Representations*, 2024.
- Shuhao Cao. Choose a transformer: Fourier or galerkin. *Advances in Neural Information Processing Systems*, 34, 2021.
- Juncai He, Xinliang Liu, and Jinchao Xu. Self-composing neural operators with depth and accuracy scaling via adaptive train-and-unroll approach. *arXiv preprint arXiv:2508.20650*, 2025.
- Xiang Cao, Qiaoqiao Ding, Xinliang Liu, Lei Zhang, and Xiaoqun Zhang. Diff-ano: Towards fast high-resolution ultrasound computed tomography via conditional consistency models and adjoint neural operators. *arXiv preprint arXiv:2507.16344*, 2025.
- Bar Lerer, Ido Ben-Yair, and Eran Treister. Multigrid-augmented deep learning preconditioners for the helmholtz equation using compact implicit layers. *SIAM Journal on Scientific Computing*, 46(5):S123–S144, 2024.
- Alexander Rudikov, Vladimir Fanaskov, Ekaterina Muravleva, Yuri M Laevsky, and Ivan Oseledets. Neural operators meet conjugate gradients: The fcg-no method for efficient pde solving. *arXiv preprint arXiv:2402.05598*, 2024.
- Enrui Zhang, Adar Kahana, Alena Kopaničáková, Eli Turkel, Rishikesh Ranade, Jay Pathak, and George Em Karniadakis. Blending neural operators and relaxation methods in pde numerical solvers. *Nature Machine Intelligence*, pages 1–11, 2024.
- Chen Cui, Kai Jiang, and Shi Shu. A neural multigrid solver for helmholtz equations with high wavenumber and heterogeneous media. *SIAM Journal on Scientific Computing*, 47(3):C655–C679, 2025.
- Yan Xie, Minrui Lv, and Chen-Song Zhang. Mgcfn: A neural multigrid solver with novel fourier neural network for high wave number helmholtz equations. In *The Thirteenth International Conference on Learning Representations*, 2025.
- Antonio Stanziola, Simon R Arridge, Ben T Cox, and Bradley E Treeby. A helmholtz equation solver using unsupervised learning: Application to transcranial ultrasound. *Journal of Computational Physics*, 441:110430, 2021.
- Xinliang Liu, Bo Xu, Shuhao Cao, and Lei Zhang. Mitigating spectral bias for the multiscale operator learning. *Journal of Computational Physics*, 506:112944, 2024.
- Nasim Rahaman, Aristide Baratin, Devansh Arpit, Felix Draxler, Min Lin, Fred Hamprecht, Yoshua Bengio, and Aaron Courville. On the spectral bias of neural networks. In *International conference on machine learning*, pages 5301–5310. PMLR, 2019.
- Antonio Stanziola, Simon Arridge, Ben T Cox, and Bradley E Treeby. A learned born series for highly-scattering media. *JASA Express Letters*, 3(5), 2023.
- Zhijun Zeng, Yihang Zheng, Youjia Zheng, Yubing Li, Zuoqiang Shi, and He Sun. Neural born series operator for biomedical ultrasound computed tomography. *arXiv preprint arXiv:2312.15575*, 2023.
- Moshe Israeli and Steven A Orszag. Approximation of radiation boundary conditions. *Journal of computational physics*, 41(1):115–135, 1981.
- Jean-Pierre Berenger. A perfectly matched layer for the absorption of electromagnetic waves. *Journal of computational physics*, 114(2):185–200, 1994.
- Chengyuan Deng, Shihang Feng, Hanchen Wang, Xitong Zhang, Peng Jin, Yinan Feng, Qili Zeng, Yinpeng Chen, and Youzuo Lin. OpenFWI: Large-scale multi-structural benchmark datasets for full waveform inversion. *Advances in Neural Information Processing Systems*, 35:6007–6020, 2022.
- Wenrui Hao, Xinliang Liu, and Yahong Yang. Newton informed neural operator for solving nonlinear partial differential equations. In *Advances in Neural Information Processing Systems*, 2024. URL <https://openreview.net/forum?id=F9mNL6vR27>.
- John P Boyd. *Chebyshev and Fourier spectral methods*. Courier Corporation, 2001.
- Lloyd N Trefethen. *Spectral Methods in MATLAB*. SIAM, Philadelphia, 2000.
- Claudio Canuto, M. Yousuff Hussaini, Alfio Quarteroni, and Thomas A Zang. *Spectral Methods: Fundamentals in Single Domains*. Springer, 2006.

A Full Derivations for CDR and Nonlinear Extensions

This appendix gives the full technical derivations deferred from the main text.

A.1 Convection-Diffusion-Reaction (Linear)

Consider

$$\mathcal{L}_{\text{cdr}}u = -\nabla \cdot (\kappa(x)\nabla u) + \mathbf{v}(x) \cdot \nabla u + \sigma(x)u = f. \quad (26)$$

Choose background constants $\kappa_0, \mathbf{v}_0, \sigma_0$ and define

$$\kappa = \kappa_0 + \delta\kappa, \quad \mathbf{v} = \mathbf{v}_0 + \delta\mathbf{v}, \quad \sigma = \sigma_0 + \delta\sigma.$$

Set

$$\mathcal{L}_{0,\text{cdr}}u := -\kappa_0\Delta u + \mathbf{v}_0 \cdot \nabla u + \sigma_0u, \quad (27)$$

and define \mathcal{V}_{cdr} by $\mathcal{L}_{\text{cdr}} = \mathcal{L}_{0,\text{cdr}} - \mathcal{V}_{\text{cdr}}$, i.e.,

$$\mathcal{V}_{\text{cdr}}u = \nabla \cdot (\delta\kappa\nabla u) - \delta\mathbf{v} \cdot \nabla u - \delta\sigma u. \quad (28)$$

Then

$$\mathcal{L}_{0,\text{cdr}}u = \mathcal{V}_{\text{cdr}}u + f. \quad (29)$$

With $G_{\text{cdr}} := \mathcal{L}_{0,\text{cdr}}^{-1}$:

$$(I - G_{\text{cdr}}\mathcal{V}_{\text{cdr}})u = G_{\text{cdr}}f = G_{\text{cdr}}\mathcal{L}_{\text{cdr}}u. \quad (30)$$

In discrete form ($A_{\text{cdr}}, V_{\text{cdr}}, G_{\text{cdr}}$):

$$I - G_{\text{cdr}}V_{\text{cdr}} = G_{\text{cdr}}A_{\text{cdr}}. \quad (31)$$

Therefore, the CDR-specific instance of the metric-matched Born Series inspired objective is

$$\mathcal{L}_{\text{bs}}^{R_{\text{cdr}}}(\theta) = \mathbb{E}_{r \sim \mathcal{D}} \frac{\|(I - G_{\text{cdr}}V_{\text{cdr}})\mathcal{M}_\theta(G_{\text{cdr}}r) - G_{\text{cdr}}r\|_2}{\|G_{\text{cdr}}r\|_2} \quad (32)$$

or equivalently

$$\mathcal{L}_{\text{bs}}^{R_{\text{cdr}}}(\theta) = \mathbb{E}_{r \sim \mathcal{D}} \frac{\|G_{\text{cdr}}A_{\text{cdr}}\mathcal{M}_\theta(G_{\text{cdr}}r) - G_{\text{cdr}}r\|_2}{\|G_{\text{cdr}}r\|_2}. \quad (33)$$

with $R_{\text{cdr}} := G_{\text{cdr}}^*G_{\text{cdr}}$. This is exactly the same template as $\mathcal{L}_{\text{bs}}^{R_\eta}$ in Section 3.3, under the substitution $(G_\eta, A, V_\eta) \mapsto (G_{\text{cdr}}, A_{\text{cdr}}, V_{\text{cdr}})$.

For periodic domains, G_{cdr} is a convolution operator with Fourier symbol

$$\widehat{G}_{\text{cdr}}(\xi) = \frac{1}{\kappa_0|\xi|^2 + i\mathbf{v}_0 \cdot \xi + \sigma_0}, \quad (34)$$

so high-frequency diffusion-dominated modes are attenuated in training. As in Helmholtz, optimizing against $G_{\text{cdr}}A_{\text{cdr}}$ instead of raw A_{cdr} improves conditioning and better matches the residual distribution in preconditioned iterations.

A.2 Nonlinear PDE via Newton-Born Linearization

For the nonlinear example

$$\mathcal{F}_{\text{nl}}(u) := -\Delta u - u^2 - f = 0, \quad (35)$$

Newton at iterate $u^{(m)}$ solves

$$J_m \delta u^{(m)} = r^{(m)}, \quad J_m := -\Delta - 2u^{(m)}, \quad r^{(m)} := -\mathcal{F}_{\text{nl}}(u^{(m)}), \quad (36)$$

followed by $u^{(m+1)} = u^{(m)} + \delta u^{(m)}$.

Discrete realization used in this work (Dirichlet + FDM + DST). For the Newton experiments in Section 4, we use homogeneous Dirichlet boundary conditions on $\Omega = [0, 1]^2$ and a five-point finite-difference discretization on interior unknowns. With $h = 1/(N + 1)$, define the discrete negative Laplacian

$$L_D u = \frac{1}{h^2} \begin{bmatrix} 0 & -1 & 0 \\ -1 & 4 & -1 \\ 0 & -1 & 0 \end{bmatrix} * u,$$

so the discrete Jacobian is

$$J_m^{\text{disc}} = L_D - 2 \text{diag}(u^{(m)}).$$

In our implementation, the $-2u^{(m)}$ term is replaced by its spatial average $-2\bar{u}^{(m)}$ in the preconditioning pipeline, where $\bar{u}^{(m)}$ denotes the spatial mean of $u^{(m)}$.

To build a Born-style preconditioned form for each Newton step, pick a reference Jacobian

$$J_{0,m} := -\Delta - 2\bar{u}^{(m)} + \alpha_m I, \quad \bar{u}^{(m)} := \text{spatial average of } u^{(m)}, \quad \alpha_m \geq 0, \quad (37)$$

whose discrete counterpart is $J_{0,m}^{\text{disc}} = L_D - 2\bar{u}^{(m)}I + \alpha_m I$ (or $J_{0,m}^{\text{disc}} \approx L_D + \alpha_m I$ in the Laplacian-dominant implementation). Equivalently, if one denotes the code-level Laplace operator by Δ_h , then $L_D = -\Delta_h$ under the sign convention used here. and define

$$V_m := J_{0,m} - J_m. \quad (38)$$

Then $J_m = J_{0,m} - V_m$, $G_m := J_{0,m}^{-1}$, and

$$(I - G_m V_m) \delta u^{(m)} = G_m r^{(m)} \Leftrightarrow I - G_m V_m = G_m J_m. \quad (39)$$

Hence the Newton-state instance of the metric-matched Born Series objective is

$$\mathcal{L}_{\text{bs}}^{R_N}(\theta) = \mathbb{E}_{(u^{(m)}, r) \sim \mathcal{D}_N} \frac{\|(I - G_m V_m) \mathcal{M}_\theta(G_m r) - G_m r\|_2}{\|G_m r\|_2}, \quad (40)$$

equivalently

$$\mathcal{L}_{\text{bs}}^{R_N}(\theta) = \mathbb{E}_{(u^{(m)}, r) \sim \mathcal{D}_N} \frac{\|G_m J_m \mathcal{M}_\theta(G_m r) - G_m r\|_2}{\|G_m r\|_2}. \quad (41)$$

where the per-state metric is $R_m := G_m^* G_m$ (so R_N denotes the Newton-trajectory family $\{R_m\}$). This is the same metric-matched objective family as $\mathcal{L}_{\text{bs}}^{R_\eta}$, with state-dependent references.

Discussion (nonlinear). The loss is computed on *linearized* systems along Newton trajectories, not directly on the nonlinear map. This has two effects:

1. It preserves the same preconditioned-coordinate advantage as the linear case (better-conditioned operator equation).
2. It aligns training with actual inference, where the solver repeatedly tackles Jacobian systems with changing $u^{(m)}$.

In practice, one may use an inner iteration

$$\delta u_{k+1}^{(m)} = \delta u_k^{(m)} + \mathcal{M}_\theta \left(G_m \left(r^{(m)} - J_m \delta u_k^{(m)} \right) \right), \quad (42)$$

then set $\delta u^{(m)} \approx \delta u_K^{(m)}$ and update $u^{(m+1)} = u^{(m)} + \delta u^{(m)}$.

B Verification: Fast Transform Implementation of Green Operators (All Cases)

We verify, case by case, when Green-operator application is fast. A concrete Fourier pseudospectral discretization recipe for L_η and G_η is provided in Appendix C.

Proposition B.1 (Transform-diagonalizable Green operators). *On a uniform grid, if the chosen reference operator has constant coefficients and compatible boundary conditions (periodic, or transform-compatible Dirichlet/Neumann), then its discrete matrix is diagonalizable by a fast trigonometric transform. Consequently, applying the corresponding discrete Green operator costs $\mathcal{O}(N \log N)$.*

Constructive verification. Let L_0 be any constant-coefficient reference operator and $G_0 = L_0^{-1}$. Under periodic boundary conditions, the discrete L_0 is block-circulant with circulant blocks, hence

$$L_0 = F^{-1}\Lambda F, \quad G_0 = F^{-1}\Lambda^{-1}F,$$

where F is the multidimensional DFT matrix and Λ contains the symbol values. Therefore

$$G_0 q = \mathcal{F}^{-1} \left(\frac{\widehat{q}}{\lambda(\xi)} \right),$$

implemented by FFT/IFFT in $\mathcal{O}(N \log N)$. For Dirichlet or Neumann boundaries, the same statement holds with sine/cosine transforms (DST/DCT), which are FFT-based and have the same complexity order. \square

Helmholtz case. With $L_\eta = -\Delta - (k_0^2 + i\eta)$, the symbol is

$$\lambda_H(\xi) = |\xi|^2 - (k_0^2 + i\eta),$$

so

$$G_\eta q = \mathcal{F}^{-1} \left(\frac{\widehat{q}}{\lambda_H(\xi)} \right).$$

Hence the Born residual $G_\eta r$ is FFT-fast under the stated boundary setting.

CDR case. With $\mathcal{L}_{0,\text{cdr}} = -\kappa_0 \Delta + \mathbf{v}_0 \cdot \nabla + \sigma_0$, the symbol is exactly (34) denominator:

$$\lambda_{\text{cdr}}(\xi) = \kappa_0 |\xi|^2 + i\mathbf{v}_0 \cdot \xi + \sigma_0.$$

Thus

$$G_{\text{cdr}} q = \mathcal{F}^{-1} \left(\frac{\widehat{q}}{\lambda_{\text{cdr}}(\xi)} \right),$$

again $\mathcal{O}(N \log N)$.

Newton-linearized system case. For the Newton experiments, we use homogeneous Dirichlet boundaries and five-point FDM on interior nodes. The reference Jacobian is diagonalized by the 2D DST-I (not periodic FFT). Writing

$$J_{0,m}^{\text{disc}} = S^{-1} \Lambda_{N,m} S,$$

with S the 2D DST-I transform, the preconditioned application is

$$G_m q = S^{-1} \left(\frac{Sq}{\lambda_{p,q}^{(m)}} \right),$$

where for the Laplacian-dominant implementation

$$\lambda_{p,q}^{(m)} \approx \frac{4}{h^2} \left[\sin^2 \left(\frac{p\pi h}{2} \right) + \sin^2 \left(\frac{q\pi h}{2} \right) \right] (+ \alpha_m \text{ if used}).$$

If the mean-reaction shift is retained, this spectrum is shifted by $\alpha_m - 2\bar{u}^{(m)}$. Therefore the Newton reference inverse is applied by DST/IDST in $\mathcal{O}(N \log N)$.

Boundary-condition note for all cases. In scattering settings, we use an absorbing layer (e.g., sponge/PML-style damping) on a finite box and choose a *constant-coefficient* reference operator on that computational domain; this is the operator inverted by FFT in the Born-inspired loss/iteration. If strict Dirichlet/Neumann boundaries are required, use DST/DCT (or FFT-based embedding), preserving near-identical complexity. In particular, the linearized Newton experiments in this paper use homogeneous Dirichlet boundaries and DST-based inversion of the FDM Laplacian reference.

C Fourier Pseudospectral Discretization of L_η and G_η

This appendix gives the concrete discretization used when L_η and $G_\eta = L_\eta^{-1}$ are implemented by FFT under periodic boundary conditions. In numerical-analysis terminology, this is a *Fourier pseudospectral* (or Fourier collocation) discretization: derivatives are represented by exact Fourier multipliers, while coefficient multiplications are applied pointwise in physical space Boyd [2001], Trefethen [2000], Canuto et al. [2006].

Periodic grid and Fourier modes. Let $\Omega = \prod_{\alpha=1}^d [0, L_\alpha)$ and use a uniform grid with N_α points in direction α :

$$x_{j_\alpha} = j_\alpha h_\alpha, \quad h_\alpha = L_\alpha / N_\alpha, \quad j_\alpha = 0, \dots, N_\alpha - 1.$$

For grid field $u_j = u(x_j)$, define the DFT coefficients \widehat{u}_n with multi-index

$$n = (n_1, \dots, n_d), \quad n_\alpha \in \left\{ -\frac{N_\alpha}{2}, \dots, \frac{N_\alpha}{2} - 1 \right\},$$

and physical wavenumbers

$$\xi_{\alpha,n} = \frac{2\pi n_\alpha}{L_\alpha}, \quad |\xi_n|^2 = \sum_{\alpha=1}^d \xi_{\alpha,n}^2.$$

Discrete symbol of L_η . For

$$L_\eta = -\Delta - (k_0^2 + i\eta), \quad \eta > 0,$$

the Fourier symbol is

$$\lambda_n = |\xi_n|^2 - (k_0^2 + i\eta),$$

so

$$\widehat{L_\eta u}_n = \lambda_n \widehat{u}_n.$$

Hence L_η is diagonal in Fourier space, and its inverse acts modewise:

$$(\widehat{G_\eta q})_n = \frac{\widehat{q}_n}{\lambda_n}.$$

Because $\eta > 0$, λ_n has nonzero imaginary part and the modal inversion is well-defined.

FFT implementation of $G_\eta q$. Given q , compute:

1. $\widehat{q} = \mathcal{F}(q)$ (FFT),
2. $\widehat{z}_n = \widehat{q}_n / \lambda_n$ (pointwise complex division),
3. $z = \mathcal{F}^{-1}(\widehat{z})$ (IFFT).

Then $z = G_\eta q$. The complexity is $\mathcal{O}(N \log N)$ with $N = \prod_\alpha N_\alpha$.

Relation to A and V_η . For heterogeneous Helmholtz,

$$Au = -\Delta u - k(x)^2 u, \quad V_\eta u = (k(x)^2 - k_0^2 - i\eta)u.$$

In Fourier pseudospectral form:

$$-\Delta u = \mathcal{F}^{-1}(|\xi|^2 \widehat{u}),$$

while $k(x)^2 u$ and $V_\eta u$ are computed pointwise in physical space. This derivative-in-Fourier / product-in-physical split is exactly the pseudospectral pattern Boyd [2001], Trefethen [2000]. For strongly non-smooth coefficients, standard de-aliasing (e.g., 2/3 truncation) can be used Canuto et al. [2006].

Boundary-condition scope. The FFT diagonalization above is exact for periodic boundaries. For homogeneous Dirichlet/Neumann boundaries, the same constant-coefficient reference operators are diagonalized by sine/cosine transforms (DST/DCT), with the same $\mathcal{O}(N \log N)$ complexity class. In this manuscript, G_η in CBS/MgNO-BS is implemented with the periodic/transform-compatible constant-coefficient reference operator to preserve fast application.

D Architectural Instantiations

The theory in the main text applies to any learned preconditioner \mathcal{M}_θ that is linear in the residual input. For completeness, we describe the concrete instantiation used across all our experiments: the Physics-Aware FNO (PA-FNO).

Physics-Aware FNO (PA-FNO). Across all test cases (including the Helmholtz equation, CDR equation, and linearized Newton systems), we employ a physics-aware nonlinear FNO, denoted **PA-FNO**. Let a (e.g., the sound velocity model v in Helmholtz, or $a = (\kappa, \mathbf{v}, \sigma)$ in CDR) be the physical coefficient fields and r the iterative residual. The module is designed to be nonlinear with respect to the coefficients a while strictly linear in the residual r , thereby satisfying the necessary preconditioned-iteration requirements. A concrete realization consistent with our implementation is formulated as:

$$\mathcal{M}_\theta(r; a) = \mathcal{P}\left(\text{LFL}\left[\text{NLFL}(\Phi_\theta(a)) \odot \text{LFL}(\Psi_\theta(r))\right]\right). \quad (43)$$

In this architecture, the input fields are first processed through designated lifting operations before passing to the core Fourier blocks. These lifting operators for the coefficient field and the residual are mathematically defined as:

$$\Phi_\theta(a) = W_a * \text{LayerNorm}(\text{pad}(a)), \quad \Psi_\theta(r) = W_r * \text{pad}(r), \quad (44)$$

and the final projection back to the original physical grid is defined as:

$$\mathcal{P}(z) = W_p * \text{unpad}(z). \quad (45)$$

Within these initial definitions, several explicit data transformations are applied to map between the physical and latent domains. The operation $\text{pad}(\cdot)$ introduces spatial padding (e.g., periodic or constant padding) along the domain boundaries. This auxiliary step is critical for mitigating boundary artifacts frequently encountered during global Fourier-domain computations. Following the latent block operations, $\text{unpad}(\cdot)$ performs the corresponding inverse truncation, removing the padded regions to restore the targeted feature field to its true spatial dimensions. For the coefficient branch, $\text{LayerNorm}(\cdot)$ applies standard layer normalization to scale and stabilize the raw physical coefficients prior to deeper network feature extraction. Furthermore, the operators W_a , W_r , and W_p denote parameterized spatial convolutions acting as channel lifters and projectors. Specifically, W_a is a 3×3 convolution designed to extract local physical features from a . Conversely, W_r and W_p are 1×1 pointwise convolutions that respectively lift the residual into a high-dimensional latent space and project the final mixed features back to the required target dimensional space.

The core of the architecture processes these lifted latent features through global convolution layers. We define the linear Fourier layer (LFL) and its nonlinear counterpart (NLFL) acting on a general latent feature field x as:

$$\text{LFL}(x) = \mathcal{F}^{-1}(\mathcal{W}_\theta^{\text{F}} \odot \mathcal{F}(x)) + \mathcal{W}_\theta^{\text{loc}} * x, \quad (46)$$

$$\text{NLFL}(x) = \varphi(\text{LFL}(x)), \quad (47)$$

where \mathcal{F} and \mathcal{F}^{-1} represent the forward and inverse discrete Fourier transforms. The tensor $\mathcal{W}_\theta^{\text{F}}$ contains learnable complex-valued weights operating on the truncated Fourier modes in the frequency domain. Meanwhile, $\mathcal{W}_\theta^{\text{loc}}$ serves as a local 1×1 spatial convolution kernel preserving high-frequency spatial information, the symbol $*$ denotes spatial convolution, and φ represents a pointwise nonlinear activation function (we utilize the Gaussian Error Linear Unit, GELU, in our implementation). In practice, multiple NLFL computing blocks are sequentially stacked to enhance the nonlinear expressive capacity of the coefficient representation. Conversely, because the LFL operation remains strictly linear, applying a single layer is sufficient to process the residual branch without redundant parameterization.